Probing the Folding and Unfolding Dynamics of Secondary and Tertiary Structures in a Three-Helix Bundle Protein†

Dung M. Vu,‡ Jeffrey K. Myers,§ Terrence G. Oas,|| and R. Brian Dyer*,‡

Biosciences Division, Mail Stop J586, Los Alamos National Laboratory, Los Alamos, New Mexico 87545, Department of Biochemistry, 5140 MRB III, Vanderbilt University Medical Center, Nashville, Tennessee 37232, and Department of Biochemistry, Box 3711, Duke University Medical Center, Durham, North Carolina 27710

Received December 8, 2003; Revised Manuscript Received January 27, 2004

ABSTRACT: Fast relaxation kinetics studies of the B-domain of staphylococcal protein A were performed to characterize the folding and unfolding of this small three-helix bundle protein. The relaxation kinetics were initiated using a laser-induced temperature jump and probed using time-resolved infrared spectroscopy. The kinetics monitored within the amide I′ absorbance of the polypeptide backbone exhibit two distinct kinetics phases with nanosecond and microsecond relaxation times. The fast kinetics relaxation time is close to the diffusion limits placed on protein folding reactions. The fast kinetics phase is dominated by the relaxation of the solvated helix ($\nu = 1632$ cm^{-1}), which reports on the fast relaxation of the individual helices. The slow kinetics phase follows the cooperative relaxation of the native helical bundle core that is monitored by both solvated ($\nu = 1632$ cm^{-1}) and buried helical IR bands ($\nu = 1652$ cm^{-1}). The folding rates of the slow kinetics phase calculated over an extended temperature range indicate that the core formation of this protein follows a pathway that is energetically downhill. The unfolding rates are much more strongly temperature-dependent indicating an activated process with a large energy barrier. These results provide significant insight into the primary process of protein folding and suggest that fast formation of helices can drive the folding of helical proteins.

Understanding the fundamental principles of protein folding requires the integration of experimental and theoretical approaches. The discovery of fast folding proteins that fold within microseconds (*1*−*6*), advances in ultrafast experimental techniques (*7*−*10*), progress in developing theoretical models for interpreting and predicting experimental results (*5*, *11*−*15*), and the ever-increasing processing power of computers are converging to make this goal attainable. Toward this end, the small size (58 residues) and simple three-helix-bundle topology of the B-domain of staphylococcal protein A (BdpA)[1] make it an ideal model for protein folding studies.

Because of its simplicity as well as its fast folding dynamics, the folding of BdpA has been scrutinized in numerous simulation studies using simplified lattice (*16*), off-lattice (*17*−*21*), atomically detailed folding (*22*−*26*) and unfolding models (*27*), and finally, more coarse-grained microdomain entities to represent helices (*4*, *28*). In most of these cases, depending on the specific details of the model, the predicted folding mechanism is either one that corresponds to a diffusion-collision model that is dependent on fast initial formation of the helices or a mechanism characterized by hydrophobic collapse with concurrent or sequential formation of helices. These differing views on the folding mechanism of BdpA clearly require further experimental studies to resolve.

Until recently, experimental kinetic studies of BdpA were limited by the millisecond and longer time constraints of conventional stopped-flow techniques (*29*). Using stopped-flow H/D pulsed exchange labeling and NMR spectroscopy, Bai et al. found that the folding of BdpA was essentially complete within the 6 ms dead time of their instrument, and no intermediates were detected (*29*). Dynamic NMR line shape analysis done by Myers and Oas revealed that the folding of BdpA occurs on the microsecond time scale (*4*). The rate extrapolated to 0 M guanidine hydrochloride was 8 μs at 37 °C. This makes it one of the fastest folding proteins yet discovered.

Using helical propensities of each of the three helices derived from experimental studies of peptide fragments of BdpA (*29*), Myers and Oas were able to show that a high helical content of the denatured state in conjunction with a diffusion−collision model can predict the folding rate of BdpA to the correct order of magnitude (*4*). The diffusion−collision model, developed by Karplus and Weaver, treats a protein as a collection of microdomains composed of secondary structure elements (i.e., the individual helices of the three-helix bundle) (*30*). The folded conformations of these microdomains (secondary structure elements) are assumed to be populated transiently in the denatured state. The microdomains diffuse and collide with one another, and

† This research was supported by the National Institutes of Health Grants GM53640 (R.B.D.) and GM45322 (T.G.O.) and postdoctoral fellowship GM18957 (J.K.M.).

* To whom correspondence should be addressed. Phone: (505) 667-4194. Fax: (505) 667-0851. E-mail: bdyer@lanl.gov.

‡ Los Alamos National Laboratory.

§ Vanderbilt University Medical Center.

|| Duke University Medical Center.

[1] Abbreviation: BdpA, B domain of protein A from *Staphylococcus aureus.*

10.1021/bi036203s CCC: $27.50
Published on Web 03/03/2004

the probability that they will coalesce into the native structure is directly related to the transient population of the folded conformation of the microdomains. From this diffusion−collision model, Myers and Oas concluded that the preorganization of nascent helix structures in the unfolded ensemble leads to the fast folding of BdpA. While this model presupposes fast formation of the individual helices of BdpA, this event was not observed experimentally.

Previous temperature jump studies on small helical peptides and helical proteins such as apomyoglobin provide a basis for understanding helix dynamics in proteins (*8*, *31*−*35*). These studies, from our group and several others, report helix relaxation lifetimes between 100 and 300 ns (*8*, *31*, *33*−*36*). The results demonstrate that helix formation can occur fast enough to be a key event at early times in the protein-folding process and that helices are capable of forming before long-range tertiary contacts are made. On the basis of these helical model studies, if fast helix formation occurs in BdpA, it is expected to occur on the submicrosecond time scale.

To probe these early events, a laser-induced temperature jump and infrared (IR) spectroscopy method was used to perturb the BdpA folding equilibrium and follow the relaxation dynamics of this protein (*7*, *8*). The amide I absorbance (1610−1680 cm^{-1}), arising primarily from the C═O stretching of the polypeptide backbone, has well-established sensitivity to secondary structure and can also provide information on the tertiary structure of proteins (*32*, *37*, *38*). Protein folding can involve structural changes as seen in changes in polypeptide backbone conformation, in hydrogen bonding, and in the solvation of the secondary structures, all of which can be probed by IR spectroscopy. The combination of laser-induced *T*-jump techniques for fast initiation of folding/unfolding events and IR spectroscopic approach for probing structural changes provide the time resolution and structure specificity necessary for determining early protein folding events (*7*, *8*).

MATERIALS AND METHODS

Protein Preparation. The plasmid containing the clone of wild-type BdpA was expressed in *Escherichia coli* BL21 (DE3) strain and purified as described previously (*4*). Typical yield was 50 mg/L pure protein. Protein purity was checked with SDS−PAGE. The purified protein was repeatedly lyophilized from D_2O (Cambridge Isotope Laboratories) to allow for complete exchange of amide protons. The protein was resuspended into a final buffer of 25 mM potassium phosphate, 50 mM NaCl at pH* 6.75 in D_2O. The protein sample was then filtered to remove aggregates and used without further purification. The pH* is the uncorrected (for D_2O) pH-meter reading at 25 °C. Sample concentrations of the protein solution used in the IR experiments were 2−4 mg/mL based on an extinction coefficient for tyrosine of 1455 M^{-1} cm^{-1} at 276 nm (*39*).

Infrared Spectroscopy and Temperature-Jump Generation. Temperature-dependent Fourier transform infrared (FTIR) spectra were obtained using a Bio-Rad model FTS-40A FTIR spectrometer. For both static and time-resolved measurements, a thermostated, dual-compartment sample cell with CaF_2 windows and a 100 μm Teflon spacer was employed to allow the separate measurements of sample and reference spectra under identical conditions. The absorbance at each temperature was computed using a single beam D_2O reference background obtained at the same temperature. The FTIR transmission spectra of the sample were recorded at a series of increasing temperatures. The equilibrium FTIR spectra were found to be fully reversible indicating the absence of aggregation at these concentrations.

The method developed in our group for studying fast protein folding dynamics has been described elsewhere (*8*, *31*). Our general approach to the rapid initiation and characterization of folding and unfolding reactions is to use a short-pulsed, laser-induced *T*-jump to shift the equilibrium between the folded and unfolded ensemble of states and to use a structure-specific IR absorbance probe to follow the secondary and tertiary structural changes. The probe for the IR measurements is a widely tunable (from 1600 to 1700 cm^{-1}) CW lead salt infrared diode laser (Laser Analytics, Laser Components Instrument Group, Inc., Wilmington MA). The source for the temperature jump is an injection-seeded, Q-switched DCR-4 Nd:YAG laser (Spectra Physics, Mountainview CA) and Raman shifter (one Stokes shift in H_2 gas) to produce the pump radiation at 2 μm (10 ns fwhm Gaussian pulse width). The wavelength of the pump pulse corresponds to the peak of a weak D_2O near-IR absorption band (ϵ = 10.1 cm^{-1} at 2 μm) and was chosen because 80% of the light is transmitted through the 100 μm path length cells used in the studies. The high transmission ensures a nearly uniform temperature profile in the approximately 250 pL (50 μm × 50 μm × 100 μm) probe-laser interaction volume. The laser energy is absorbed by water (D_2O), and the temperature of the volume of water reaches its maximum value within ∼20 ns (twice the fwhm of the pump pulse) since temperature thermalization and diffusion within water occur on subnanosecond time scales. The diffusion of heat out of the interaction volume takes about 20 ms in our cells. The size of the *T*-jump was calibrated using the change in D_2O absorbance with temperature, which acts as an internal thermometer in the range of 1632−1700 cm^{-1} (*31*). The *T*-jump was determined to within 2 °C.

The transient absorption of the probe beam in the sample is monitored using a fast (50 MHz) HgCdTe IR detector (Kolmar, Newburyport, MA), and the digitization of the detector signal is performed by a Tektronix 7612D digitizer (Beaverton, OR). The net instrument response time (a convolution of the heating and detector response times) is ∼23 ns. Transient changes in the absorbance of the protein or solvent system were averaged for 3000−5000 laser shots at 10 Hz. The D_2O buffered reference measurements provide information needed for both background subtraction and *T*-jump calibration.

Analysis of the Fast Kinetics Data. Analysis of the protein relaxation kinetics at the earlier nanosecond time scales was carried out by deconvolving the instrument response from the observed kinetics. Deconvolution of the instrument response is possible because it is determined concurrently with each sample measurement under the exact same conditions. Using a macro created in IGOR (Wavemetrics Inc., Lake Oswego OR), we fit the observed sample relaxation kinetics as a function of the instrument response convolved with an exponential decay. The instrument response function for the system is taken to be the derivative of the reference trace, normalized to have an integral function of one at the maximum of the reference trace. Normalizing

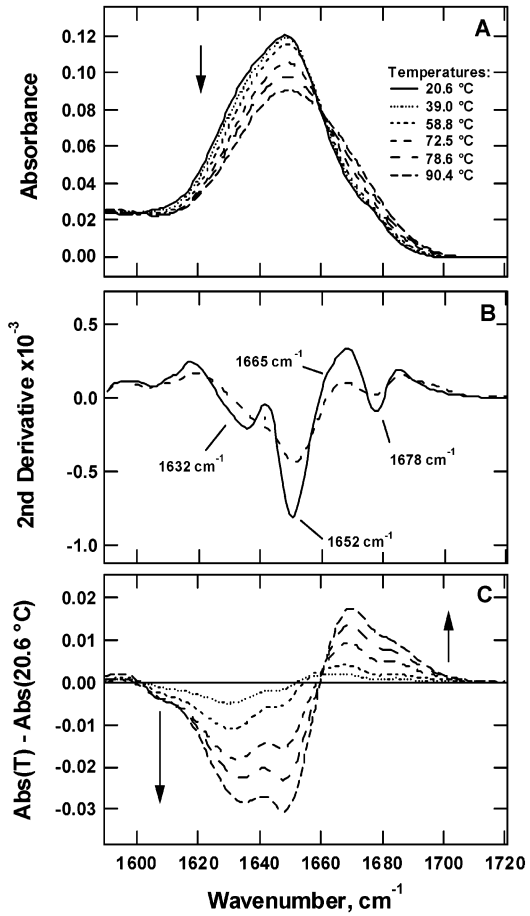

FIGURE 1: FTIR absorbance spectra (A) of BdpA in D_2O buffered solution (4 mg/mL in 25 mM sodium phosphate, 50 mM NaCl, uncorrected pH* = 6.75) in the region of the amide I′ band, as a function of temperature from 20.6 to 90.4 °C. The absorbance at each temperature is computed using a single beam D_2O background obtained at the same temperature. The arrow indicates the direction of increasing temperature, from 20.6 to 90.4 °C. Panel B shows the second-derivative spectra at 29.8 (solid line) and 72.5 °C (dashed line). The major structural components of amide I′ are observed near 1632, 1652, 1665, and 1678 cm^{-1}. Panel C shows the FTIR difference spectra of BdpA. The difference spectra are generated by subtracting the spectrum at 20.6 °C from the spectrum at each temperature. The arrows indicate direction of increasing temperature. The primary difference peaks occur near 1632, 1652, and 1668 cm^{-1}.

the instrument response is necessary so that amplitudes represent changes in absorbance. The decay function used is an exponential decay function with the formula (A exp($-kT$)), where A and k are the change in absorbance and the rate, respectively.

RESULTS

The thermal equilibrium unfolding of BdpA was followed using FTIR spectroscopy, and the structural changes were monitored at the amide I′ region (Figure 1A, the prime denotes the frequencies of the deuterated amide group). The amide I′ absorption envelope is centered around 1646 cm^{-1} at low temperatures but broadens and shifts to higher frequency as the temperature increases (Figure 1A). Due to considerable overlap of the structural components in the raw absorbance spectra, identifying the equilibrium changes of the various structural components is difficult. Resolution enhancement of the equilibrium FTIR spectra (at 29.8 and 72.5 °C) via second-derivative analysis reveals four major amide I′ subcomponents at 1632, 1652, 1665, and 1678 cm^{-1} (Figure 1B). Difference spectra were generated by subtracting the spectrum at 20.6 °C from the spectrum at each temperature to show the equilibrium changes of these various subcomponents upon thermal denaturation (Figure 1C). As the temperature is increased, the troughs at 1632, 1652, and 1678 cm^{-1} deepen, with the concomitant growth of a broad peak centered between 1665 and 1675 cm^{-1}. These observations serve as a guide for band assignments.

Previous peptide model and protein studies in D_2O have shown that disordered structures generally exhibit a broad amide I′ absorbance centered between 1665 and 1675 cm^{-1} (*31, 40, 41*) and that the band near 1678 cm^{-1} arises from the turn structures (*37, 42*). The characteristic frequency range for a native helix protected from solvent by the tertiary fold ("buried" helix) is 1650−1655 cm^{-1} (*37, 42, 43*). In the absence of protection by tertiary structure, the helix backbone experiences a greater exposure to water and exhibits a "red" shift to lower frequencies (1630 to 1640 cm^{-1}) (*31, 38, 44, 45*). In their defining experiment, Manas and co-workers separately labeled the amide carbonyl groups of exposed alanines and buried leucines of the dimeric α-helical coiled-coil GCN4-P1′ with ^{13}C and showed that the lower frequency shifts of the ^{13}C alanines (1585 cm^{-1}) compared to ^{13}C leucines (1606 cm^{-1}) permitted the distinction between α-helical regions that were solvent-exposed from those that were buried (*45*). Therefore, the lower frequency helical structure is labeled "solvated". Because the environment of the helices in BdpA is similar to that of the coiled-coil GCN4-P1′, the two troughs in the difference spectra (Figure 1C) near 1632 and 1652 cm^{-1} are assigned to the solvated and buried helix, respectively. The broad peak at 1668 cm^{-1} and the trough at 1678 cm^{-1} are attributed to the disordered and turn structures, respectively.

The temperature-dependent FTIR absorbances of BdpA demonstrate the sensitivity of the amide I′ C═O stretches to the conformational changes that take place during the unfolding of this protein. The disappearance of the solvated helix (signal at 1632 cm^{-1}) and buried helix contributions (signal at 1652 cm^{-1}) and the appearance of the disordered structure contribution (signal at 1668 cm^{-1}) can be followed in the melting curves of Figure 2. Both the buried helix and solvated helix exhibit a cooperative melting transition near 73.3 ± 1 °C. This transition midpoint temperature is similar to that observed with far-UV CD measurements (signal at 222 nm, T_m = 72.5 ± 0.1 °C). The enthalpic (ΔH) and entropic (ΔS) contributions from the melt of the buried helix derived from a two-state transition analysis are shown in Table 1. The Gibbs free energies (ΔG) for this process are also calculated at the various temperatures indicated to allow for comparison with other experimental results (*4, 29*). While the melting curves of these two structural components show sigmoidal transitions near the same temperature range, their overall melting behaviors differ. The thermal denaturation of the buried helix appears cooperative with an apparent two-state transition. In contrast, the melting of the solvated helix shows a cooperative transition convolved with a broad, underlying transition. Clearly there is more than one process occurring in the melting of the solvated helix component of BdpA. We have performed a more complete analysis of this melt below, by taking into account the kinetics results for

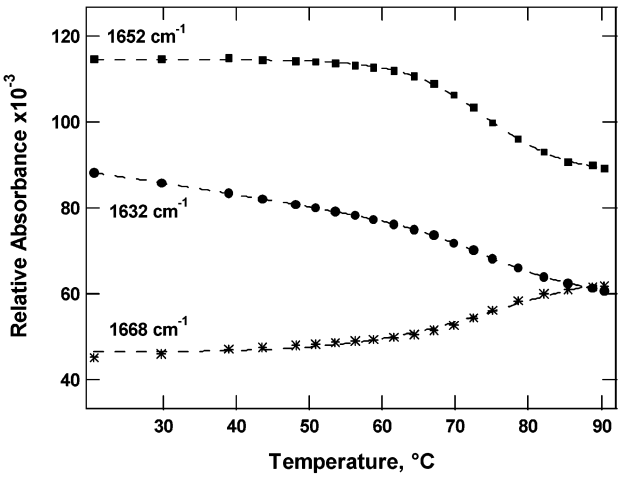

FIGURE 2: Thermal denaturation of BdpA monitored at 1632 (●, solvated helix), 1652 (■, buried helix), and 1668 cm^{-1} (∗, disordered structure). The 1652 cm^{-1} fit is based on a two-state model with a melting temperature (T_m) of 73.3 ± 1 °C, a value that is close to that observed in the far-UV CD (222 nm) thermal denaturation curve. The 1632 cm^{-1} fit shows a convolution of the single, narrow and broad, underlying functions, which suggests that at least two processes are occurring in the unfolding of BdpA. The narrow part of the transition at 1632 cm^{-1} shows a T_m similar to that observed for the 1652 cm^{-1} melt.

Table 1: Equilibrium Thermodynamic Parameters for Folding of BdpA

	buried helix 1652 cm^{-1}	Bai et al.[29]	Myers and Oas[4]
T_m (°C)	73.3 ± 1		72.5 ± 0.1
ΔH (kcal mol^{-1})	−46.8 ± 1		−50.4 ± 0.2
ΔS (cal mol^{-1} K^{-1})	−135.1 ± 3		
ΔG (kcal mol^{-1}), 20 °C	−7.2 ± 1	−7.0 ± 1	
ΔG (kcal mol^{-1}), 37 °C	−4.9 ± 1		−4.3 ± 0.2

the solvated helix component. The melting curve of the disordered structure (signal at 1668 cm^{-1}) shows contributions from the melts of both the solvated and buried helices. It is clear from these results that the folding and unfolding of BdpA is not a simple two-state process. These equilibrium temperature-dependent observations also serve as a guide for the *T*-jump kinetics experiments.

The relaxation kinetics of BdpA were initiated by a laser-induced *T*-jump, and the kinetics were probed in the amide I′ region in a series of jumps sampling temperatures along the unfolding transition. We explored a range of final temperatures from strongly folding to strongly unfolding conditions. Figure 3 shows the transient IR absorbance of the two vibrational frequencies corresponding to the helical structures (solvated helix, 1632 cm^{-1}, and buried helix, 1652 cm^{-1}) with temperature jumps starting from the folded region (60.0 °C) to near the transition midpoint (73.1 °C). To accurately determine the kinetics at the earlier time scale, the instrument response was deconvolved from the observed fast relaxation using the deconvolution procedure described in Materials and Methods. By resolving the fast relaxation kinetics with the deconvolution procedure, two kinetics phases, separated by 2 orders of magnitude in time, can be deduced from these transient responses. The transient at 1632 cm^{-1} has contributions from both the fast kinetics phase (57%) and the slow kinetics phase (43%) with relaxation times of 90 ± 10 ns and 9.7 ± 1 μs, respectively. The

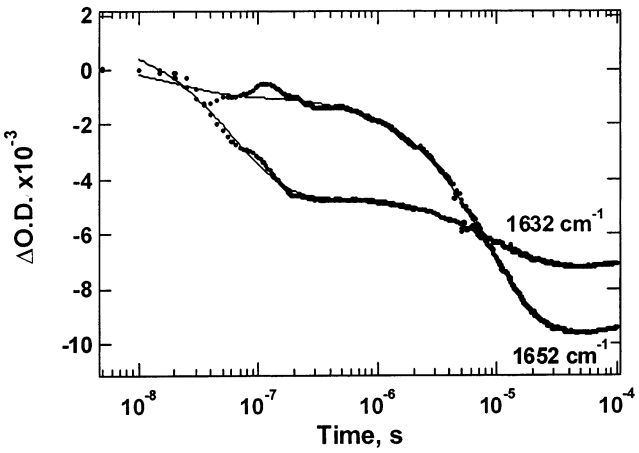

FIGURE 3: Transient IR responses for *T*-jumps from 60.0 to 73.1 °C at 1632 and 1652 cm^{-1}. The D_2O background responses have been subtracted from these data. Two kinetics phases are clearly present in both transient responses. The fit to a biexponential function convolved with the instrument response at 1632 cm^{-1}, shown by the solid line, yields 90 ± 10 ns (57%) and 9.7 ± 1 μs (43%) for the two lifetimes. The 1652 cm^{-1} transient is dominated by the slow kinetics phase with a relaxation time of 8.6 ± 1 μs (92%). A small fast kinetics phase is also present with relaxation time of 200 ± 50 ns (8%).

transient at 1652 cm^{-1} is dominated by the slow kinetics phase (92%) but still has a small contribution from the fast phase (8%). The relaxation times for the fast and slow kinetics phases are 200 ± 50 ns and 8.6 ± 1 μs. The experimental apparatus can detect structural changes beyond several milliseconds, and yet no slower processes were observed, indicating that the relaxation of BdpA is complete within the 9−10 μs time.

A more complete analysis of the equilibrium melt is possible using the relaxation kinetics results to help deconvolve the two observed transitions. Although the thermal melt of the buried helix component shows only a single, narrow transition and the kinetics of this component are dominated by the slow relaxation phase, a small amplitude fast phase is also observed with this structural probe. This result suggests that another process is occurring on this fast time scale despite the absence of an intermediate in the equilibrium melt (Figures 2 and 3). The detection of this intermediate can be better resolved when the thermal melt of the solvated helix component is compared with the corresponding kinetics results (Figures 2 and 3). The amplitudes of each kinetics phase follow the different parts of this equilibrium melt. The amplitude of the fast kinetics phase follows the broad part of the melt, whereas the amplitude of the slow kinetics phase follows the narrow part. Therefore, we can use the fast kinetics phase amplitude to deconvolve the broad underlying component of the melt from the narrow component. In Figure 4, the amplitude contributions of the fast relaxation kinetics at the various temperature jumps are shown mapped onto the equilibrium melt of the solvated helix. When these fast kinetics amplitude contributions at the higher temperatures are extrapolated to the lower temperature region, a relatively broad and noncooperative transition is revealed. This transition was fit to a broad sigmoid function and a T_m near 58 ± 5 °C was determined. The melting transition of this broad contribution shows similar characteristics to those previously observed with short helical peptides (*31*).

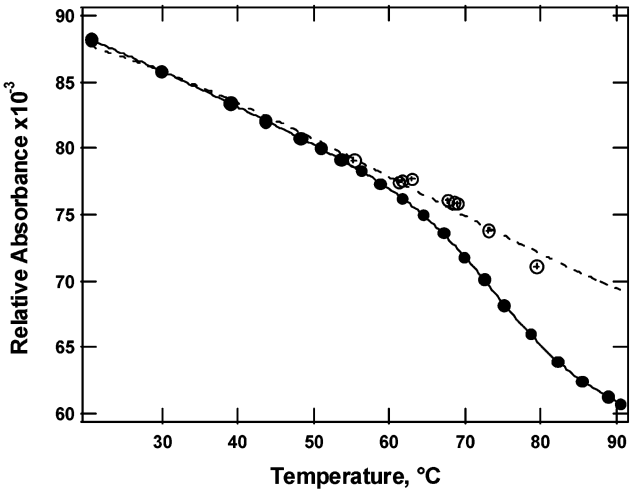

FIGURE 4: Broad transition extrapolation of the solvated helix equilibrium melt. The amplitude contributions of the fast relaxation kinetics at the various *T*-jumps (crosshatched circles) are shown mapped onto the thermal equilibrium melt of the solvated helix (closed circles). The amplitudes of the fast kinetics contributions are extrapolated back to the lower temperature region. A relatively broad and noncooperative transition is observed with a melting temperature near 58 ± 5 °C.

The simplest kinetics model that can account for the two relaxation times observed requires three structural ensembles of BdpA. Therefore, we have modeled the folding and unfolding of BdpA as a simple three-state reaction:

$$\mathrm{U} \underset{k_{-1}}{\overset{k_{\mathrm{obs1}}\ k_1}{\rightleftharpoons}} \mathrm{I} \underset{k_{-2}}{\overset{k_{\mathrm{obs2}}\ k_2}{\rightleftharpoons}} \mathrm{F}$$

where U, I, and F represent the unfolded, intermediate, and folded ensembles. Although the *T*-jump rapidly changes the equilibrium conditions in the direction of the unfolded state, because of the position of the equilibrium, the rates that are measured have contributions from both folding and unfolding kinetics (*32*). The microscopic folding and unfolding rates were calculated based on the assumption that $k_{\mathrm{obs1}} \gg k_{\mathrm{obs2}}$:

$$k_{\mathrm{obs1}} = k_1 + k_{-1}$$

$$k_{\mathrm{obs2}} = k_2\left(\frac{k_1}{k_1 + k_{-1}}\right) + k_{-2}$$

where k_{obs1} and k_{obs2} are the observed fast and slow relaxation rates, k_1 and k_{-1} are the microscopic folding and unfolding rates for the fast process, and k_2 and k_{-2} are the microscopic folding and unfolding rates for the slower process. These relationships show that the equilibration of the slow process (I ↔ F) is coupled to the rapid equilibration of the fast relaxation process (U ↔ I). Because the 1652 cm^{-1} component (buried helix) follows the global unfolding of BdpA (Figure 2), the equilibrium constant (K_T) derived from this melt was taken to reflect the overall unfolding of BdpA. K_T is also the product of the individual steps, $K_T = K_{\mathrm{eq1}}K_{\mathrm{eq2}}$. The equilibrium constant of the fast relaxation, K_{eq1}, was approximated from the extrapolation of the broad component of the solvated helix as presented in Figure 4. Therefore the equilibrium constant derived for the slower process was calculated from the ratio of K_T/K_{eq1}.

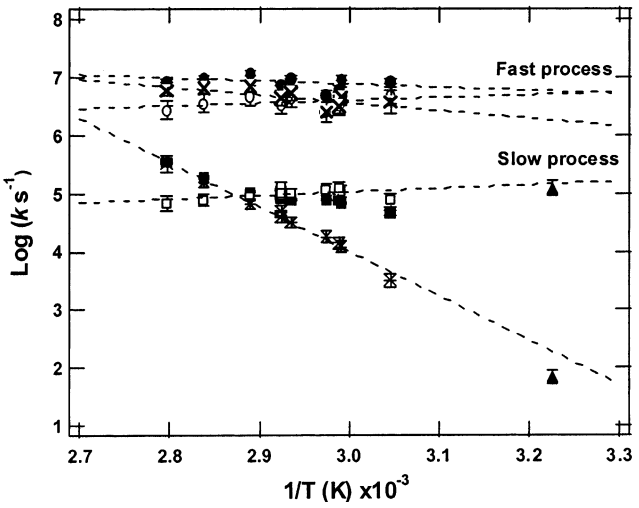

FIGURE 5: Temperature dependence of the fast relaxation (●) and slow relaxation kinetics (■) monitored at 1632 cm^{-1}. The 1/*T* axis represents the final temperatures reached during the *T*-jump. The microscopic folding (○) and unfolding rates (×) from the fast relaxation process and the folding (□) and unfolding rates (∗) from the slower relaxation process were calculated from a three-state folding model. The activation parameters derived from these plots are given in Table 2. The folding and unfolding rates of BdpA (▲) reported from Myers and Oas (*4*) are also shown on the Arrhenius plots.

Table 2: Kinetics Parameters for Folding and Unfolding of BdpA

	$\Delta H^{\ddagger}$ kcal mol^{-1}	$\Delta S^{\ddagger}$ cal mol^{-1} K^{-1}	$\Delta G^{\ddagger}$ kcal mol^{-1}, 20 °C	$\Delta G^{\ddagger}$ kcal mol^{-1}, 37 °C
k_1	−2.1 ± 2	−14.2 ± 5.8	2.1 ± 2	2.3 ± 2
k_{-1}	6.1 ± 2	10.3 ± 5.3	3.1 ± 2	2.9 ± 2
k_2	−2.7 ± 1.8	−23.2 ± 5.2	4.1 ± 1.8	4.5 ± 1.8
k_{-2}	34.9 ± 1.6	85.1 ± 4.6	10.0 ± 1.6	8.5 ± 1.6

An Arrhenius plot of the observed relaxation kinetics of the two processes, as well as the respective calculated folding and unfolding rates, is shown in Figure 5. The enthalpies ($\Delta H^{\ddagger}$) and entropies ($\Delta S^{\ddagger}$) of activation for folding and unfolding of both of these process are shown in Table 2. The activation parameters are calculated according to transition state theory:

$$k = k_0 \exp\left(\frac{\Delta S^{\ddagger}}{R}\right) \exp\left(\frac{-\Delta H^{\ddagger}}{RT}\right)$$

The determination of the activation entropy requires an estimate of the preexponential factor, k_0. A recent study of the end-to-end contact rates in polypeptides found a limiting rate for minimum loop formation (i.e., formation of *i*, *i* + 3 interactions) of 2 × 10^8 s^{-1} (*46*). Krieger et al. postulate that this rate is a fundamental property of polypeptide chains and represents a reasonable preexponential factor for folding reactions. The Gibbs free energies of activation ($\Delta G^{\ddagger}$) are also calculated at the various temperatures and shown in Table 2. The folding rate (k_f = 120 000 s^{-1}) and unfolding rate (k_u = 68 s^{-1}) of BdpA at 37 °C reported from Myers and Oas from their NMR experiments (*4*) are also shown in the Arrhenius plots.

DISCUSSION

The global folding of BdpA has been reported to be very fast (extrapolated τ_f = 8 μs at 37 °C) as determined from

NMR relaxation dynamics (*4*). Thus BdpA is one of the fastest folding proteins discovered to date. In the present study, in addition to observing similar microsecond folding times, a much faster process is also evident that precedes the formation of the tertiary helical bundle.

Since the amide I′ mode is due primarily to the polypeptide carbonyl (C═O) stretching vibration, it reports on secondary structure conformations and can also provide information on the tertiary structure of proteins. For BdpA, two types of helices can be clearly distinguished within the amide I′ absorbance band; these helices have been identified as the buried helix (helix protected from solvent by the tertiary fold) and the solvated helix (helix interacting with solvent in the absence of protection by tertiary structure). Therefore, the buried helix is mainly reporting on the hydrophobic side of the helical bundle whereas the solvated helix is reporting on the hydrophilic side of the helical bundle as well as the individual helices.

We first consider the relaxation kinetics and melting behavior of BdpA monitored at the buried helix component. The melting behavior of the buried helix component shows a single cooperative transition with a T_m near 73.3 °C and relaxation times that are dominated by a microsecond relaxation phase ($\tau_{obs} = 8.6\ \mu s$ at 73.1 °C). Since the buried helix band tracks the formation of the helical bundle core, this relaxation phase corresponds to the formation of the tertiary fold. While the presence of an intermediate is not evident from the thermal equilibrium melt, the detection of a small amplitude fast kinetics phase suggests that there is a short-lived intermediate. This short-lived intermediate becomes more pronounced when the relaxation dynamics and the thermal equilibrium unfolding of BdpA are tracked with the solvated helix band. We attribute the relaxation of this short-lived intermediate to the helix−coil transition for two reasons: (1) the solvated helix band has a weakly cooperative melting behavior that is similar to that observed with the melting of helical peptide models (*31, 35*), and (2) the fast relaxation shows the characteristic lifetime observed in peptide models and helical proteins. Helix relaxation lifetimes obtained from temperature jump studies on peptide models from our group and several others are between 100 and 300 ns (*8, 31, 33*−*36*). These lifetimes are insensitive to helix length and composition. In addition, *T*-jump studies of two helical proteins, apomyoglobin (*32, 47*) and the villin headpiece subdomain (*6*), report similar fast nanosecond relaxation lifetimes. In both of these cases, the fast relaxation lifetimes were attributed to the helix−coil transition.

The observation of two relaxation processes requires at least three states to describe the folding and unfolding reactions of BdpA. The simplest kinetics model that allows us to incorporate all of these observations is the following:

$$U \underset{}{\overset{\tau_{R1} = 90\ ns}{\rightleftharpoons}} I \overset{\tau_{R2} = 9\ \mu s}{\rightleftharpoons} F$$

where U represents the unfolded ensemble and I represents the ensemble with nascent helices, but with no packed core. F represents the folded three-helix-bundle ensemble. The indicated relaxation times reflect experimental data taken near the midpoint of the global unfolding transition (73.1 °C). The U to I transition corresponds to the fast formation of individual helices, whereas the I to F transition represents the packing of the helices together to form the three-helix bundle. Thus the first step is dominated by the fast (characteristic) rate of formation of the individual helices, whereas the second step reflects the slow process of diffusing the helices together, squeezing out the water, and packing the side chains together. It is only in the second step that the solvent-protected helix is formed and thus the observed kinetics monitored at the buried helix wavelength are dominated by the slow process.

In this model of the folding of BdpA, fast formation of individual helices precedes the formation of the tertiary helical bundle. Numerous studies by our group and several others have shown that helices can certainly form fast enough to precede formation of long-range tertiary contacts (*8, 31, 33*−*36*). Relaxation of the solvated helix in both peptides and proteins has a characteristic rate ($\sim 10^7\ s^{-1}$). The microsecond relaxation time observed for BdpA is similar to the lifetime observed for the cooperative packing of the side chains of the individual helices in apomyoglobin and the villin headpiece subdomain (*6, 32, 48*). This model is fully consistent with the diffusion−collision mechanism for the folding of BdpA as postulated in experimental and theoretical studies (*4, 28*). Myers and Oas predicted the folding rate of BdpA in good agreement with experiment using a diffusion−collision model that featured a significant helical content in the denatured state, based on the results of Bai et al. (*4, 29*). A similar diffusion−collision analysis carried out by Islam and co-workers also predicted the fast folding rate of BdpA that was dependent on a high helical content in the unfolded state (*28*). Therefore, while both of these studies project that the fast formation of BdpA depends on nascent formation of the helices, we provide direct evidence for this diffusion−collision model by detecting fast helix formation that precedes the formation of long-range tertiary contacts.

We tested the validity of the three-state model by simulating the time-dependent concentrations of U, I, and F using the coupled differential equations that describe the three-state reaction. While the simulated relaxation rates reproduce the experimental rates within experimental error, the predicted amplitude of the fast kinetics phase relative to the slow kinetics phase is consistently smaller than what we observe experimentally. A quantitative comparison of the amplitudes of the IR transients with the simulated concentrations was not possible, because the overlapping IR bands result in contributions from all three species (U, I, and F) at each probe wavelength. Nevertheless, probe wavelengths could be selected for which one species is dominant (e.g., I dominates at 1632 cm^{-1}) for comparison to the simulated time-dependent concentration of this species. Comparison of the time-dependent concentration of I to the IR transient at 1632 cm^{-1} showed a distinctly larger amplitude of the observed fast component than what is predicted by the model. A plausible explanation for this discrepancy is another helix−coil transition that is off-pathway and hence is not being accounted for in our simple diffusion−collision model. Such an off-pathway transition likely involves a peripheral part of the structure that does not affect the three-helix core, such as the N-terminal "tail" structure of the protein. The NMR structure of BdpA shows that the N-terminal sequence is somewhat flexible and disordered; hence it may form a transient helical structure that undergoes a fast helix−coil (off-pathway) transition (*49*).

The folding and unfolding rates of the fast and slow kinetics phases derived from the three-state model exhibit linear Arrhenius behavior over an extended temperature range. The Arrhenius-type behavior and negative activation enthalpy observed for the formation of individual helices of BdpA have been observed for other small helical peptide systems (*35*, *50*, *51*). A small barrier to unfolding is also observed in these systems (*35*, *50*, *51*). The folding and unfolding rates of the helical bundle core calculated over an extended temperature range also exhibit linear Arrhenius behavior. Nonlinear Arrhenius behavior is sometimes observed in protein folding; for example, Rnase A, lysozyme, chymotrypsin inhibitor, and barnase all exhibit a parabolic dependence of ln *k* on reciprocal temperature, which has been attributed to the difference in heat capacity between the unfolded and transition states ($\Delta C_p^{\ddagger}$) (*52*−*54*). The $\Delta C_p^{\ddagger}$ term likely originates from the large decrease in exposure of hydrophobic surfaces to water on going from the unfolded state to the transition state. In the case of BdpA, however, the linearity of the Arrhenius behavior translates into a small or zero $\Delta C_p^{\ddagger}$ value, suggesting that the folding reaction does not involve significant burial of hydrophobic residues in the transition state. This observation supports the diffusion−collision model because the transition state in this model consists of folded but solvated individual helices and therefore does not likely have much buried hydrophobic surface area. The activation parameters derived from the Arrhenius analysis (Table 2) yield further insight into the folding mechanism. The formation of the helices and the helical bundle core of BdpA follow a pathway that is enthalpically downhill with primarily an entropic barrier. Both steps exhibit substantial entropic barriers as expected for the loss of configurational entropy that occurs in the helix nucleation and helix−helix association processes. The unfolding rates are much more strongly temperature-dependent indicating that the unfolding of BdpA is an activated process with a large enthalpic barrier.

These results provide significant insight into the primary processes of protein folding and suggest that kinetic traps are not expected to dominate the folding time for fast-folding helical proteins. In addition, this is the first direct observation of fast helix formation supporting a diffusion−collision folding mechanism.

ACKNOWLEDGMENT

D. Vu thanks Hector Rodriguez for helpful discussions and assistance with the kinetics simulation.

REFERENCES

1. Huang, G. S., and Oas, T. G. (1995) Submillisecond folding of monomeric lambda repressor, *Proc. Natl. Acad. Sci. U.S.A. 92*, 6878−6882.
2. Spector, S., and Raleigh, D. P. (1999) Submillisecond folding of the peripheral subunit-binding domain, *J. Mol. Biol. 293*, 763−768.
3. Mayor, U., Johnson, C. M., Daggett, V., and Fersht, A. R. (2000) Protein folding and unfolding in microseconds to nanoseconds by experiment and simulation, *Proc. Natl. Acad. Sci. U.S.A. 97*, 13518−13522.
4. Myers, J. K., and Oas, T. G. (2001) Preorganized secondary structure as an important determinant of fast protein folding, *Nat. Struct. Biol. 8*, 552−558.
5. Snow, C. D., Nguyen, H., Pande, V. S., and Gruebele, M. (2002) Absolute comparison of simulated and experimental protein-folding dynamics, *Nature 420*, 102−106.
6. Kubelka, J., Eaton, W. A., and Hofrichter, J. (2003) Experimental tests of villin subdomain folding simulations, *J. Mol. Biol. 329*, 625−630.
7. Callendar, R. H., Dyer, R. B., Gilmanshin, R., and Woodruff, W. H. (1998) Fast events in protein folding: The time evolution of primary processes, *Annu. Rev. Phys. Chem. 49*, 173−202.
8. Dyer, R. B., Gai, F., Woodruff, W. H., Gilmanshin, R., and Callender, R. H. (1998) Infrared studies of fast events in protein folding, *Acc. Chem. Res. 31*, 709−716.
9. Nölting, B. (1999) *Protein Folding Kinetics: Biophysical Methods*, pp 51−76, Springer, New York.
10. Myers, J. K., and Oas, T. G. (2002) Mechanism of fast protein folding, *Annu. Rev. Biochem. 71*, 783−815.
11. Shea, J.-E., and Brooks, C. L., III (2001) From folding theories to folding proteins: A review and assessment of simulation studies of protein folding and unfolding, *Annu. Rev. Phys. Chem. 52*, 499−535.
12. Clementi, C., García, A. E., and Onuchic, J. N. (2003) Interplay among tertiary contacts, secondary structure formation and side-chain packing in the protein folding mechanism: All-atom representation study of protein L, *J. Mol. Biol. 326*, 933−954.
13. Weikl, T. R., and Dill, K. A. (2003) Folding rates and low-entropy-loss routes of two-state proteins, *J. Mol. Biol. 329*.
14. Mayor, U., Guydosh, N. R., Johnson, C. M., Grossman, J. G., Sato, S., Jas, G. S., Freund, S. M. V., Alonso, D. O. V., Daggett, V., and Fersht, A. R. (2003) The complete folding pathway of a protein from nanoseconds to microseconds, *Nature 421*, 863−867.
15. Pande, V. S., Baker, I., Chapman, J., Elmer, S. P., Khaliq, S., Larson, S. M., Rhee, Y. M., Shirts, M. R., Snow, C. D., Sorin, E. J., and Zagrovic, B. (2003) Atomistic protein folding simulations on the submillisecond time scale using worldwide distributed computing, *Biopolymers 68*, 91−109.
16. Kolinski, A., and Skolnick, J. (1994) Monte Carlo simulations of protein folding. II. Application to protein A, ROP, and crambin, *Proteins 18*, 353−366.
17. Zhou, Y., and Karplus, M. (1999) Interpreting the folding kinetics of helical proteins, *Nature 401*, 400−403.
18. Zhou, Y., and Karplus, M. (1999) Folding of a model three-helix bundle protein: a thermodynamics and kinetic analysis, *J. Mol. Biol. 293*, 917−951.
19. Shea, J., Onuchic, J. N., and Brooks, C. L., III (1999) Exploring the origins of topological frustration: Design of a minimally frustrated model of fragment B of protein A, *Proc. Natl. Acad. Sci. U.S.A. 96*, 12512−12517.
20. Berriz, G. F., and Shakhnovich, E. I. (2001) Characterization of the folding kinetics of a three-helix bundle protein via a minimalist langevin model, *J. Mol. Biol. 310*, 673−685.
21. Favrin, G., Irback, A., and Wallin, S. (2002) Folding of a small helical protein using hydrogen bonds and hydrophobicity forces, *Proteins 18*, 99−105.
22. Boczko, E. M., and Brooks, C. L., III (1995) First-principles calculation of the folding free energy of a three-helix bundle protein, *Science 269*, 393−396.
23. Guo, Z., Brooks, C. L., III, and Boczko, E. M. (1997) Exploring the folding free energy surface of a three-helix bundle protein, *Proc. Natl. Acad. Sci. U.S.A. 94*, 10161−10166.
24. Ghosh, A., Elber, R., and Scheraga, H. A. (2002) An atomically detailed study of the folding pathways of protein A with the stochiastic difference equation, *Proc. Natl. Acad. Sci. U.S.A. 99*, 10394−10398.
25. Jang, S., Kim, E., Shin, S., and Pak, Y. (2003) Ab intio folding of helix bundle proteins using molecular dynamics simulations, *J. Am. Chem. Soc. 125*, 14841−14846.
26. García, A. E., and Onuchic, J. N. (2003) Folding a protein in a computer: An atomic description of the folding/unfolding of protein A, *Proc. Natl. Acad. Sci. U.S.A. 100*, 13898−13903.
27. Alonso, D. O. V., and Daggett, V. (2000) Staphylococcal protein A: Unfolding pathways, unfolded states and differences between the B and E domains, *Proc. Natl. Acad. Sci. U.S.A. 97*, 133−138.
28. Islam, S. A., Karplus, M., and Weaver, D. L. (2002) Application of the diffusion-collision model to the folding of three-helix bundle proteins, *J. Mol. Biol. 318*, 199−215.

29. Bai, Y., Karimi, A., Dyson, H. J., and Wright, P. P. (1997) Absence of a stable intermediate on the folding pathway of protein A, *Protein Sci. 6*, 1449−1457.
30. Karplus, M., and Weaver, D. L. (1994) Protein folding dynamics: the diffusion-collision model and experimental data, *Protein Sci. 3*, 650−668.
31. Williams, S., Causgrove, T. P., Gilmanshin, R., Fang, K. S., Callender, R. H., Woodruff, W. H., and Dyer, R. B. (1996) Fast events in protein folding: helix melting and formation in a small peptide, *Biochemistry 35*, 691−697.
32. Gilmanshin, R., Williams, S., Callender, R. H., Woodruff, W. H., and Dyer, R. B. (1997) Fast events in protein folding: relaxation dynamics of secondary and tertiary structure in native apomyoglobin, *Proc. Natl. Acad. Sci. U.S.A. 94*, 3709−3713.
33. Thompson, P. A., Munoz, V., Jas, G., Henry, E., Eaton, W., and Hofrichter, J. (2000) The helix-coil kinetics of a heteropeptide, *J. Phys. Chem. B 104*, 378−389.
34. Lednev, I. K., Karnoup, A. S., Sparrow, M. C., and Asher, S. A. (2001) Transient UV Raman spectroscopy finds no crossing barrier between the peptide α-helix and fully random conformation, *J. Am. Chem. Soc. 123*, 2388−2392.
35. Werner, J. H., Dyer, R. B., Fesinmeyer, R. M., and Andersen, N. H. (2002) Dynamics of the primary process of protein folding: Helix nucleation, *J. Phys. Chem. B 106*, 487−494.
36. Huang, C. Y., Getahun, Z., Zhu, Y. J., Klemke, J. W., DeGrado, W. F., and Gai, F. (2002) Helix formation via conformation diffusion search, *Proc. Natl. Acad. Sci. U.S.A. 99*, 2788−2793.
37. Susi, H., and Byler, D. M. (1986) Resolution-enhanced Fourier transform infrared spectroscopy of enzymes, *Methods Enzymol. 130*, 290−311.
38. Haris, P. I., and Chapman, D. (1995) The conformational analysis of peptides using Fourier transform IR spectroscopy, *Biopolymers 37*, 251−263.
39. Pace, C. N., Vajdos, F., Fee, L., Grimsley, G., and Gray, T. (1995) How to measure and predict the molar absorption coefficient of a protein, *Protein Sci. 4*, 2411−2423.
40. Venyaminov, S. Y., and Kalnin, N. N. (1990) Quantitative IR spectrophotometry of peptide compounds in water (H_2O) solutions. 2. Amide absorption-bands of polypeptides and fibrous proteins in alpha-coil, beta-coil, and random-coil conformations, *Biopolymers 30*, 1259−1271.
41. Reinstadler, D., Fabian, H., Backman, J., and Naumann, D. (1996) Refolding of thermally and urea-denatured ribonuclease A monitored by time-resolved FTIR spectroscopy, *Biochemistry 35*, 15822−15830.
42. Arrondo, J. L., Blanco, F. J., Serrano, L., and Goni, F. M. (1996) Infrared evidence of a beta-hairpin peptide structure in solution, *FEBS Lett. 384*, 35−37.
43. Jackson, M., and Mantsch, H. H. (1995) The use and misuse of FTIR spectroscopy in the determination of protein-structure, *Crit. Rev. Biochem. Mol. Biol. 30*, 95−120.
44. Reisdorf, W. C., and Krimm, S. (1996) Infrared amide I′ band of the coiled coil, *Biochemistry 35*, 1383−1386.
45. Manas, E. S., Getahun, Z., Wright, W. W., DeGrado, W. F., and Vanderkooi, J. M. (2000) Infrared spectra of amide groups in α-helical proteins: Evidence for hydrogen bonding between helices and water, *J. Am. Chem. Soc. 122*, 9883−9890.
46. Krieger, F., Fierz, B., Bieri, O., Drewello, M., and Kiefhaber, T. (2003) Dynamics of unfolded polypeptide chains as model for the earliest steps in protein folding, *J. Mol. Biol. 332*, 265−274.
47. Gilmanshin, R., Callender, R. H., and Dyer, R. B. (1998) The core of apomyoglobin E-form folds at the diffusion limit, *Nat. Struct. Biol. 5*, 363−365.
48. Gilmanshin, R., Dyer, R. B., and Callender, R. H. (1997) Structural heterogeneity of the various forms of apomyoglobin: implications for protein folding, *Protein Sci. 6*, 2134−2142.
49. Gouda, H., Torigoe, H., Saito, A., Sato, M., Arata, Y., and Shimada, I. (1992) Three-dimensional solution structure of the B domain of staphylococcal protein A: comparisons of the solution and crystal structures, *Biochemistry 31* (40), 9665−9672.
50. Lednev, I. K., Karnoup, A. S., Sparrow, M. C., and Asher, S. (1999) Nanosecond UV resonance Raman examination of initial steps in α-helical secondary structure evolution, *J. Am. Chem. Soc. 121*, 4076−4077.
51. Lednev, I. K., Karnoup, A. S., Sparrow, M. C., and Asher, S. (1999) α-Helix peptide folding and unfolding activation barriers: A nanosecond UV resonance Raman study, *J. Am. Chem. Soc. 121*, 8074−8086.
52. Hagerman, P. J., and Baldwin, R. L. (1976) Quantitative treatment of kinetics of folding transition of Ribonuclease A, *Biochemistry 15*, 1462−1473.
53. Chen, B., Baase, W. A., and Schellman, J. A. (1989) Low-temperature unfolding of a mutant phage T4 lysozyme. 2. Kinetic investigations, *Biochemistry 28*, 691−699.
54. Oliveberg, M., Tan, Y.-J., and Fersht, A. R. (1995) Negative activation enthalpies in the kinetics of protein folding, *Proc. Natl. Acad. Sci. U.S.A. 92*, 8926−8929.

BI036203S